Progress In Electromagnetics Research B, Vol. 59, 1–18, 2014

Multilayered Superlenses Containing CsBr or Active Medium for Subwavelength Photolithography

Li-Hao Yeh and Jean-Fu Kiang*

Abstract—The characteristics of periodic multilayered near-field superlenses are analyzed and optimized, using the dispersion relation derived from an effective medium theory and the transfer function in the spectral domain. The k_z'-k_x and k_z''-k_x contours are used to explain and predict the spectral width, amplitude and phase of the transfer function. Superlenses containing CsBr or active layers are proposed to reduce image distortion or to compensate for the propagation loss, respectively. The parameters of the superlenses can be optimized by simulations to resolve half-pitch features down to $\lambda/36$ using CsBr layers, and $\lambda/20$ using active layers.

1. INTRODUCTION

Wave propagation through negative-ϵ (ENG), negative-μ (MNG) or double-negative (DNG) materials has been widely studied [1]. Pendry pointed out that ENG and MNG materials can converge TM and TE wave, respectively; and a DNG material can converge both TE and TM waves [2]. The conventional diffraction limit on resolution can be broken using a slab of these materials [2], which is also called a superlens.

Superlenses built with ENG materials have been proposed in the optical or UV bands [3–13]. Surface plasmon polaritons (SPP's) can be excited around the interface between an ENG layer and a matching layer, the latter is usually made of a double-positive (DPS) material with the same $|\epsilon|$ as the ENG layer. The image resolution can be improved by involving these SPP's.

When applied to photolithography, half-pitch of 60 nm ($\sim \lambda/6$ at $\lambda = 365$ nm) can be resolved with a single-layer silver superlens [4], and half-pitch of 20 nm ($\sim \lambda/10$ at $\lambda = 193$ nm) can be resolved with a single-layer superlens with an index matching layer [3]. A superlens composed of multiple layers of ENG (metal) and positive-ϵ (dielectric) materials is claimed to out-perform a single-layer superlens in resolution [5–12]. By interleaving metal layers with dielectric layers, with both thinner than that of a single-layer superlens, the attenuation is reduced and the resolution is improved [5, 6]. In [7, 12], a transfer matrix method is applied to study the performance of multilayered superlenses, which can resolve half-pitch of 50 nm ($\sim \lambda/7$ at $\lambda = 365$ nm).

A periodic multilayered structure, made of metal and dielectric layers, can be described as an equivalent homogeneous anisotropic medium [8–10], which is a function of the thickness ratio and the permittivity of the constituent layers. Half-pitch of 40 nm ($\sim \lambda/11$ at $\lambda = 442$ nm) can be resolved [9]. The dispersion relation of the equivalent homogeneous medium can be used to predict the propagation direction of the wave.

The aforementioned superlenses operate in the near-field region, where the evanescent waves are not severely attenuated. Alternatively, far-field superlenses (FSL), having a longer separation between the mask and the image plane to prevent mask damage, can also break the conventional diffraction limit [13–16]. For example, half-pitch of $\lambda/8$ has been resolved using the FSL [14]. A common approach

Received 31 December 2013, Accepted 24 February 2014, Scheduled 7 March 2014

* Corresponding author: Jean-Fu Kiang (jfkiang@ntu.edu.tw).
The authors are with the Department of Electrical Engineering, National Taiwan University, Taipei, Taiwan 106, R.O.C.

is to fabricate a grating between an ENG layer and a DPS layer. The garting is designed to induce Floquet's modes of the evanescent waves and propagate the information of the latter. Hyperlens and hybrid-superlens have also been proposed for microscopic applications [17, 18].

In this paper, both the k_z'-k_x and k_z''-k_x contours, derived from the dispersion relation, are explored to predict the transfer function of multilayered superlenses. The resolution of a superlens is fine-tuned with the transfer function thus obtained. Layers made of CsBr layer and active medium are also proposed to further improve the phase and attenuation characteristics of the superlens. This paper is organized as follows: a layered-medium formulation is briefly described in Section 2, an effective medium thoery for multiple layers is briefly reviewed in Section 3. Simulations on superlenses containing periodic cells, CsBr layers and active layers are presented in Sections 4, 5 and 6, respectively. The tolerance analysis of these superlens designs is presented in Section 7, and some conclusions are drawn in Section 8.

2. BRIEF REVIEW OF LAYERED-MEDIUM FORMULATION

Figure 1 depicts the configuration of a multilayered medium on top of a double-slot mask. The field of TM polarization is assumed, with the field specified as $H_y(x, z = 0) = H_0 = 1$, on the slots at $|x + w/2| \le a/2$ and $|x - w/2| \le a/2$. The H_y component at $z = 0$ and in layer (ℓ), respectively, can be expressed in the spectral domain as [19]

$$\begin{aligned} H_y(x,0) &= \frac{1}{2\pi}\int_{-\infty}^{\infty} dk_x e^{-jk_x x}\tilde{H}_y(k_x) \\ H_{\ell y}(x,z) &= \frac{1}{2\pi}\int_{-\infty}^{\infty} dk_x e^{-jk_x x}\left[H_{\ell\cup}e^{-jk_{\ell z}z_\ell} + H_{\ell\cap}e^{jk_{\ell z}z_\ell}\right], \quad 1 \le \ell \le N \\ H_{(N+1)y}(x,z) &= \frac{1}{2\pi}\int_{-\infty}^{\infty} dk_x e^{-jk_x x}H_{(N+1)\cup}e^{-jk_{(N+1)z}z_{N+1}} \end{aligned} \tag{1}$$

where $z_\ell = z - h_{\ell-1}$. Define, at $z_\ell = d_\ell$, a reflection coefficient, $R_{\ell\cap} = H_{\ell\cap}e^{jk_{\ell z}d_\ell}/H_{\ell\cup}e^{-jk_{\ell z}d_\ell}$. Then impose the continuity conditions at $z_\ell = d_\ell$, to derive a recursive relation as

$$R_{\ell\cap} = \frac{R_{\ell(\ell+1)} + R_{(\ell+1)\cap}e^{-2jk_{(\ell+1)z}d_{\ell+1}}}{1 + R_{\ell(\ell+1)}R_{(\ell+1)\cap}e^{-2jk_{(\ell+1)z}d_{\ell+1}}} \tag{2}$$

where

$$R_{\ell(\ell+1)} = \frac{\epsilon_{\ell+1}k_{\ell z} - \epsilon_\ell k_{(\ell+1)z}}{\epsilon_{\ell+1}k_{\ell z} + \epsilon_\ell k_{(\ell+1)z}} \tag{3}$$

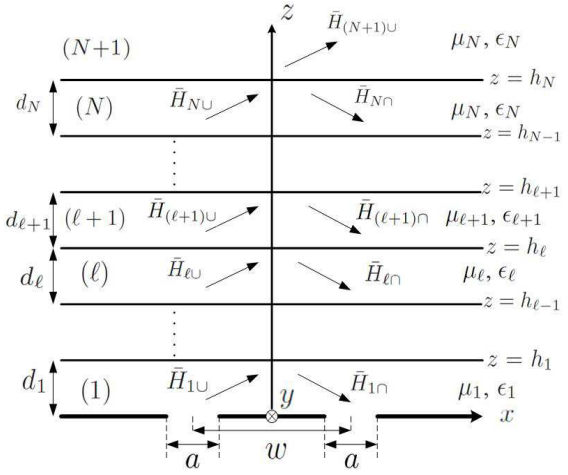

Figure 1. Configuration of a multilayered medium on top of a double-slot mask, with the image plane at $z = h_N$.

is the Fresnel reflection coefficient between layers ℓ and $\ell+1$. By substituting

$$R_{N\cap} = \frac{\epsilon_{N+1}k_{Nz} - \epsilon_N k_{(N+1)z}}{\epsilon_{N+1}k_{Nz} + \epsilon_N k_{(N+1)z}} = R_{N(N+1)} \tag{4}$$

into (2), with $\ell = N-2$, $R_{(N-2)\cap}$ is obtained. Repeating (2) with $\ell = N-3, N-4, \ldots$, all the $R_{\ell\cap}$'s are obtained. By imposing the continuity conditions, the amplitude, $H_{\ell\cup}$, are derived as

$$\begin{aligned} H_{1\cup} &= \frac{\tilde{H}_y(k_x)}{1 + R_{1\cap}e^{-2jk_{1z}d_1}} \\ H_{(\ell+1)\cup} &= H_{\ell\cup}\frac{(1+R_{\ell\cap})e^{-jk_{\ell z}d_\ell}}{1 + R_{(\ell+1)\cap}e^{-2jk_{(\ell+1)z}d_{\ell+1}}} \\ H_{(N+1)\cup} &= H_{N\cup}(1+R_{N\cap})e^{-jk_{Nz}d_N} \end{aligned}$$

Next, define the transfer function at the top boundary of each layer as

$$T_\ell(k_x) = \frac{H_{\ell\cup}(1+R_{\ell(\ell+1)})e^{-jk_{\ell z}d_\ell}}{\tilde{H}_y(k_x)}, \quad 1 \le \ell \le N \tag{5}$$

Hence, the magnetic field in the image plane, $z = h_N$, can be expressed as

$$H_y(x, z = h_N) = \int_{-\infty}^{\infty} dk_x e^{-jk_x x}\tilde{H}_y(k_x)T_N(k_x)$$

3. BRIEF REVIEW OF EFFECTIVE MEDIUM THEORY

Figure 2 depicts a periodic multilayered medium, intended to function as a superlens. An approximate approach, based on the characteristic matrix [20], has been applied to derive an equivalent homogeneous anisotropic medium to a periodic multilayered medium [8].

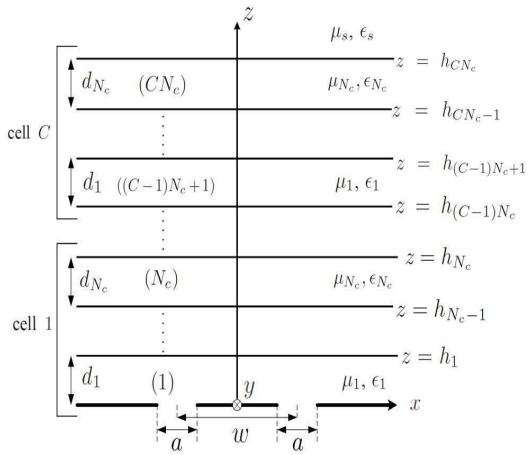

Figure 2. Configuration of a periodic multilayered medium on top of a double-slot mask, with the image plane at $z = h_{CN_c}$.

3.1. Approximation Approach

The characteristic matrix, $M(k_x, \epsilon_\ell, d_\ell)$, of a homogeneous medium is derived as [8]

$$M(k_x, \epsilon_\ell, d_\ell) = \begin{bmatrix} \cos(k_{\ell z}d_\ell) & \dfrac{j\omega\epsilon_{\ell r}}{k_{\ell z}}\sin(k_{\ell z}d_\ell) \\ \dfrac{jk_{\ell z}}{\omega\epsilon_{\ell r}}\sin(k_{\ell z}d_\ell) & \cos(k_{\ell z}d_\ell) \end{bmatrix} \tag{6}$$

where ϵ_ℓ and d_ℓ are the permittivity and thickness, respectively, of the medium; and $k_{\ell z}$ satisfies the dispersion relation

$$k_x^2 + k_{\ell z}^2 = k_0^2 \epsilon_{\ell r} \tag{7}$$

If the multilayered structure is composed of C cells, with each cell consisting of N_c layers of homogeneous medium, the characteristic matrix of a single cell takes the product form [8]

$$M_{\text{cell}}(k_x) = M(k_x, \epsilon_1, d_1) \ldots M(k_x, \epsilon_{N_c}, d_{N_c}) \tag{8}$$

which can be expressed in terms of the effective parameters, ϵ_{rx}, ϵ_{rz} and k_{az}, as [8]

$$M_{\text{cell}}(k_x) = \begin{bmatrix} \cos(k_{az} d_c) & \dfrac{j\omega\epsilon_{rx}}{k_{az}} \sin(k_{az} d_c) \\ \dfrac{j k_{az}}{\omega \epsilon_{rx}} \sin(k_{az} d_c) & \cos(k_{az} d_c) \end{bmatrix} \tag{9}$$

where $d_c = d_1 + \ldots + d_{N_c}$ is the total thickness of one cell.

The effectiveness of this expression has been verified in [8], for the case of $N_c = 2$, under the assumption that $k_{\ell z} d_\ell \ll 1$ and $k_{az} d_c \ll 1$; which implies $\cos(k_{\ell z} d_\ell) \simeq 1$, $\cos(k_{az} d_c) \simeq 1$, $\sin(k_{\ell z} d_\ell) \simeq k_{\ell z} d_\ell$, and $\sin(k_{az} d_c) \simeq k_{az} d_c$. Thus, (8) and (9) can be approximated as

$$M_{\text{cell}}(k_x) \simeq \begin{bmatrix} 1 & j\omega \displaystyle\sum_{\ell=1}^{N_c} d_\ell \epsilon_{\ell r} \\ \dfrac{j}{\omega} \displaystyle\sum_{\ell=1}^{N_c} \dfrac{k_{\ell z}^2 d_\ell}{\epsilon_{\ell r}} & 1 \end{bmatrix} \tag{10}$$

$$M_{\text{cell}}(k_x) \simeq \begin{bmatrix} 1 & j\omega\epsilon_{rx} d_c \\ \dfrac{j k_{az}^2 d_c}{\omega \epsilon_{rx}} & 1 \end{bmatrix} \tag{11}$$

Next, equate (10) with (11), with the dispersion relation in (7), to derive

$$\frac{k_x^2}{\epsilon_{rz}} + \frac{k_{az}^2}{\epsilon_{rx}} = k_0^2 \tag{12}$$

where

$$\epsilon_{rx} = \frac{\displaystyle\sum_{\ell=1}^{N_c} d_\ell \epsilon_{\ell r}}{d_c}, \quad \frac{1}{\epsilon_{rz}} = \frac{\displaystyle\sum_{\ell=1}^{N_c} \frac{d_\ell}{\epsilon_{\ell r}}}{d_c} \tag{13}$$

which is the extended version of that in [8]. These effective parameters of a single cell depend only on the thickness ratio among layers in a cell, as long as $k_{\ell z} d_\ell \ll 1$ and $k_{az} d_c \ll 1$.

The characteristic matrix of the whole medium, composed of C cells, can be expressed in terms of these effective parameters as [8]

$$M_t(k_x) = \begin{bmatrix} \cos(k_{az} d) & \dfrac{j\omega\epsilon_{rx}}{k_{az}} \sin(k_{az} d) \\ \dfrac{j k_{az}}{\omega \epsilon_{rx}} \sin(k_{az} d) & \cos(k_{az} d) \end{bmatrix} \tag{14}$$

where $d = C d_c$ is the thickness of the whole medium. If $k_{az} d \ll 1$, the previous approximation can also be applied to derive the effective parameters of the whole medium.

3.2. Eigenvalue Approach

An alternative approach is to diagonalize $M_t = M_{\text{cell}}^C$ into [8]

$$M_t(k_x) = \begin{bmatrix} 1 & 1 \\ p & q \end{bmatrix} \begin{bmatrix} e^{-jk_{ez}d} & 0 \\ 0 & e^{jk_{ez}d} \end{bmatrix} \begin{bmatrix} 1 & 1 \\ p & q \end{bmatrix}^{-1} \tag{15}$$

where k_{ez} is the eigenvalue. The prediction using the eigenvalue approach is expected to be close to that using the approximation approach as C is large while the total thickness of the medium is fixed.

3.3. Properties of k_z-k_x Contours

The dispersion relation can be presented as k'_z-k_x and k''_z-k_x contours, where $k_z = k'_z + jk''_z$. The normals to the k'_z-k_x contours suggest the wave propagation direction, while the normal to the k''_z-k_x contours suggest the wave attenuation direction.

When the approximation approach is applied, the dispersion relation of a multilayered structure can be expressed as (12). If the permittivities of all layers are real, the k'_z-k_x and k''_z-k_x contours will be a hyperbola or an ellipse, depending on the values of ϵ_{rx} and ϵ_{rz}.

If both ϵ_{rx} and ϵ_{rz} are positive, the k'_z-k_x and k''_z-k_x contours are ellipses and hyperbolas, respectively. Wave components at large k_x have a large k''_z, and attenuate significantly with z. If one of ϵ_{rx} and ϵ_{rz} is negative, and the other is positive, the k'_z-k_x contours are hyperbolas, and the k''_z-k_x contours are ellipses. The slope of the asymptote to a hyperbola is determined as [8]

$$\frac{dk_{az}}{dk_x} = \pm\sqrt{\left|\frac{\epsilon_{rx}}{\epsilon_{rz}}\right|}$$

When the layers are slightly lossy, ϵ_{rx} and ϵ_{rz} become complex numbers of $\epsilon_{rx} = \epsilon'_{rx} + j\epsilon''_{rx}$ and $\epsilon_{rz} = \epsilon'_{rz} + j\epsilon''_{rz}$, respectively; and the asymptotes of the k'_z-k_x and k''_z-k_x contours can be expressed as

$$\begin{aligned} k'_{az} &= \pm k_x\sqrt{\frac{|\epsilon_{rx}||\epsilon_{rz}| - (\epsilon'_{rx}\epsilon'_{rz} + \epsilon''_{rx}\epsilon''_{rz})}{2|\epsilon_{rz}|^2}} \\ k''_{az} &= \pm k_x\sqrt{\frac{|\epsilon_{rx}||\epsilon_{rz}| + (\epsilon'_{rx}\epsilon'_{rz} + \epsilon''_{rx}\epsilon''_{rz})}{2|\epsilon_{rz}|^2}} \end{aligned} \tag{16}$$

which can be used to predict the shape of the transfer functions later. The asymptotes to the k''_z-k_x contours have not been discussed in the literatures.

3.4. Transfer Function of Periodic Multilayered Structure

Periodic multilayered structures have been used to implement superlenses [7, 9, 13]. The k'_z-k_x and k''_z-k_x contours, derived from the dispersion relation of the multilayered structure, can be used to explain the properties of the transfer function and to design a better superlens.

In [8, 10], the transfer function of an anisotropic metal-dielectric layered structure has been derived. However, their definition of the transfer function is slightly different from ours. As shown

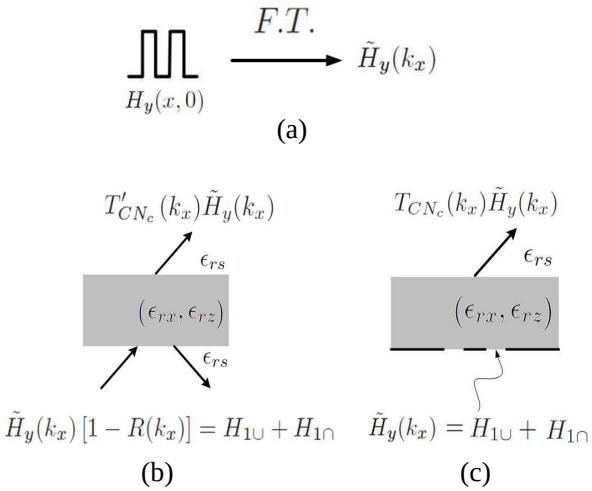

Figure 3. (a) Fourier transform of the input magnetic field, $H_y(x, 0)$, representing the original image. (a) Simulation configuration in [8, 10]. (b) Simulation configuration in this paper, assuming a photomask in front of the superlens.

in Figure 3(b) [8, 10], the wave representing the original image, $H_y(x, 0)$, is incident from below the superlens, and part of the wave is reflected at the interface. In this paper, a photo-mask is assumed at the interface, as shown in Figure 3(c), and the total field at $z = 0$ is the original image, $H_y(x, 0)$.

The transfer function of the configuration in Figure 3(c) is derived as

$$T_{CN_c}(k_x) = \frac{1}{\cos(k_{az}d) + j\dfrac{\epsilon_{rx}k_{sz}}{\epsilon_{rs}k_{az}}\sin(k_{az}d)} \tag{17}$$

where ϵ_{rs} and k_{sz} are the relative permittivity and the z-component of the wavevector, respectively, of the medium above the superlens. Similarly, the transfer function of the configuration in Figure 3(b) is derived as [8, 10]

$$T'_{CN_c}(k_x) = \frac{2}{2\cos(k_{az}d) + j\left(\dfrac{\epsilon_{rs}k_{az}}{\epsilon_{rx}k_{sz}} + \dfrac{\epsilon_{rx}k_{sz}}{\epsilon_{rs}k_{az}}\right)\sin(k_{az}d)} \tag{18}$$

At large k_x, (17) and (18) can be approximated as

$$\begin{aligned} T_{CN_c}(k_x) &\simeq \frac{2}{\left(1 + \dfrac{\epsilon_{rx}k_{sz}}{\epsilon_{rs}k_{az}}\right)e^{jk'_{az}d - k''_{az}d}} \\ T'_{CN_c}(k_x) &\simeq \frac{4}{\left(2 + \dfrac{\epsilon_{rx}k_{sz}}{\epsilon_{rs}k_{az}} + \dfrac{\epsilon_{rs}k_{az}}{\epsilon_{rx}k_{sz}}\right)e^{jk'_{az}d - k''_{az}d}} \end{aligned} \tag{19}$$

The magnitude of both transfer functions is close to a constant if the slope of the k''_z-k_x asymptote is small over the range of interest. The slope of the k'_z-k_x asymptote determines the phase response of the transfer functions.

At small k_x, $k_{az}d \ll 1$, and the transfer functions can be approximated as

$$\begin{aligned} T_{CN_c}(k_x) &\simeq \frac{1}{1 + j(\epsilon_{rx}/\epsilon_{rs})k_{sz}d} \\ T'_{CN_c}(k_x) &\simeq \frac{2}{2 + j(\epsilon_{rx}/\epsilon_{rs})k_{sz}d + \dfrac{\epsilon_{rs}\left(k_0^2 - k_x^2/\epsilon_{rz}\right)d}{k_{sz}}} \end{aligned} \tag{20}$$

which are nearly independent of k_x if $\epsilon_{rx} \simeq 0$, especially for T_{CN_c}.

By changing the ratio of layer thicknesses, the transfer function, T'_{CN_c}, can have a small slope of k'_z-k_x contours over a wider range of k_x, especially when $\epsilon_{rx} = 0$ or $1/\epsilon_{rz} = 0$ [10]. In that case, the waves can propagate in a direction more perpendicular to the layer interfaces, resulting in a better image resolution. From (16), the slope of the k''_z-k_x asymptote is correlated to that of the k'_z-k_x asymptote. Thus, both asymptotes can have small slopes, implying a wider k_x bandwidth of the transfer function.

4. SUPERLENSES MADE OF TWO-LAYER CELLS

Consider a periodic multilayered superlens with a total thickness of $d = 80\,\text{nm}$. The wavelength of the incident light is assumed 365 nm. Each cell is composed of two layers ($N_c = 2$), with the thickness ratio, $d_1/d_2 = 1$. Layer 1 is made of PMMA ($\epsilon_{\text{PMMA}} = (2.3013 - j0.0014)\epsilon_0$) [7], and layer 2 is made of silver ($\epsilon_{\text{Ag}} = (-2.7 - j0.23)\epsilon_0$) [21]. Both materials are commonly used in the multilayered superlenses at this wavelength. On top of the superlens is SU-8, a photo-resist ($\epsilon_s = 2.78\epsilon_0$) [22].

Figure 4 shows the effect of cell number on the k'_z-k_x and k''_z-k_x contours, the transfer function, and the recovered image of the PMMA/Ag periodic multilayered superlens. When more cells are chosen, the k_{ez}-k_x contours becomes closer to the k_{az}-k_x contours; and the transfer function becomes closer to the closed form in (17). The relevant parameters associated with Figure 4, using the approximation approach (AA), are listed in Table 1.

A smaller slope of asymptote to the k_z''-k_x contour implies a smaller decaying rate for high k_x components. Hence, the transfer function with a larger C in Figure 4(d) tends to have a wider spectral width in k_x. A smaller slope of asymptote to the k_z'-k_x contour makes the phase of the transfer function closer to a linear function of k_x, which implies less distortion to the original image intensity.

Figure 5 shows the effect when the dielectric and the metal layers are switched. The k_z-k_x contours remain the same, but the transfer functions become different due to the change of boundary conditions. The reversed order of Ag/PMMA produces a worse transfer function because Ag, in direct contact with the photo mask, tends to prevent the wave components from propagating through it. As a result, the field in the first Ag layer decays much faster in the Ag/PMMA arrangement than that in the first PMMA layer in the PMMA/Ag arrangement. The difference becomes less significant as C becomes large, as shown in Figure 6.

In order to expand the low-k_x band of the transfer function, the slope of the k_z''-k_x asymptote is preferred to be as small as possible, which can be achieved if $|\epsilon_{rx}| \to 0$ or $|1/\epsilon_{rz}| \to 0$.

Next, we try to adjust the ratio, d_1/d_2, at $C = 8$, aiming to tune the real part of ϵ_{rx} and $1/\epsilon_{rz}$ to

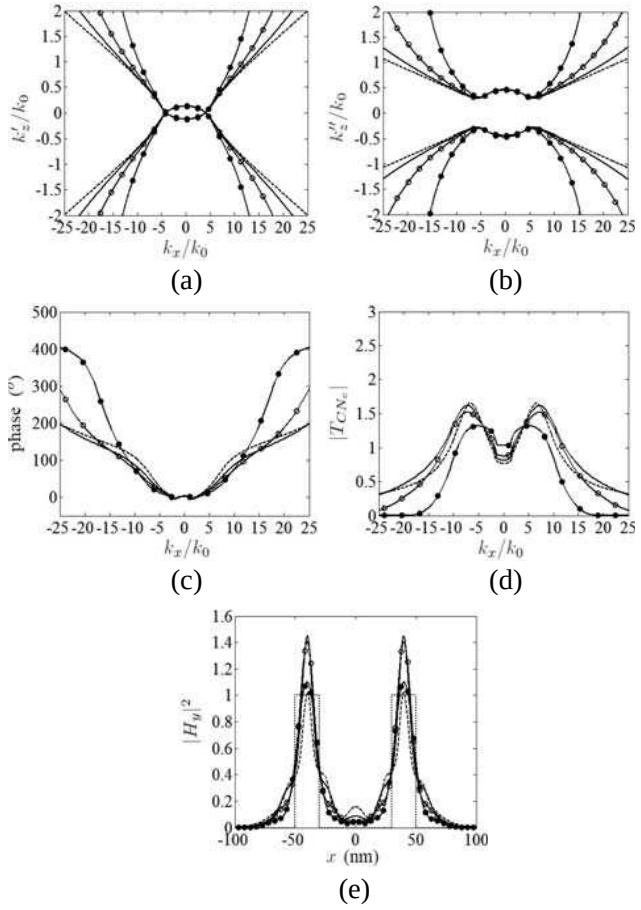

Figure 4. Effect of cell number on the characteristics of periodic multilayered superlenses: (a) k_z'-k_x contour, (b) k_z''-k_x contour, (c) phase of transfer function, (d) amplitude of transfer function, (e) recovered image. —•—: $C = 4$ (EA), —○—: $C = 8$ (EA), —: $C = 16$ (EA), ---: (AA) $N_c = 2$, $\epsilon_1 = (2.3013 - j0.0014)\epsilon_0$, $\epsilon_2 = (-2.7 - j0.23)\epsilon_0$, $d = 80\,\text{nm}$, $a = 20\,\text{nm}$, $w = 80\,\text{nm}$.

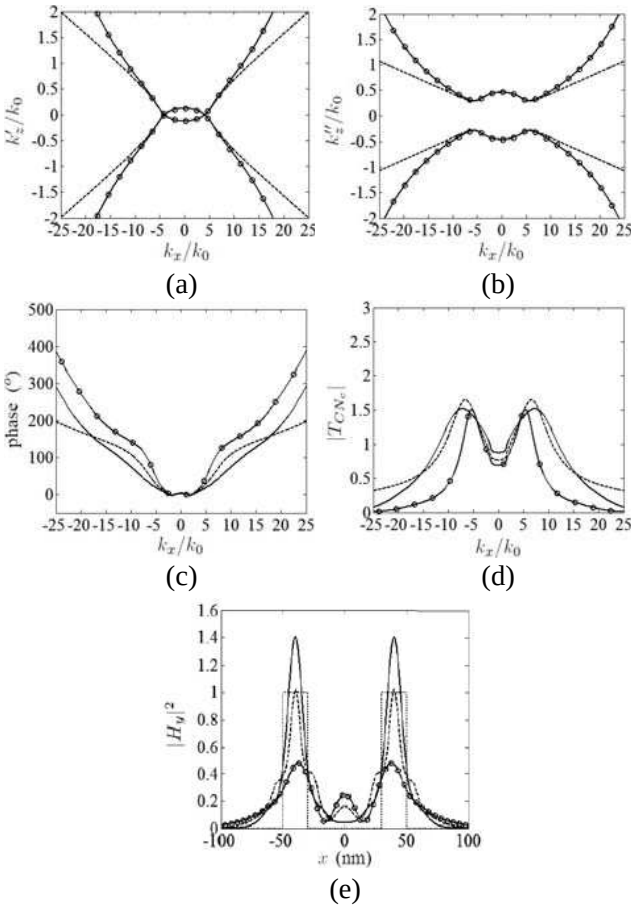

Figure 5. Effect of layer order on the characteristics of the periodic multilayered superlens: (a) k_z'-k_x contour, (b) k_z''-k_x contour, (c) phase of transfer function, (d) amplitude of transfer function, (e) recovered image. —: $C = 8$ (EA), $d_1/d_2 = 1$, with $\epsilon_1 = (2.3013 - j0.0014)\epsilon_0$, $\epsilon_2 = (-2.7 - j0.23)\epsilon_0$, —○—: $C = 8$ (EA), $d_1/d_2 = 1$, with $\epsilon_1 = (-2.7 - j0.23)\epsilon_0$, $\epsilon_2 = (2.3013 - j0.0014)\epsilon_0$, ---: (AA), $d_1/d_2 = 1$, $N_c = 2$, $d = 80\,\text{nm}$, $a = 20\,\text{nm}$, $w = 80\,\text{nm}$.

Table 1. Effective parameters and slope of asymptotes, using the approximate approach (AA).

	ϵ_{rx}	ϵ_{rz}	dk'_z/dk_x	dk''_z/dk_x
Figure 4	-0.1994 $-j0.1157$	24.4609 $-j11.5606$	±0.0817	±0.0429
Figure 7, $d_1/d_2 = 1.173$	$-j0.1066$	14.57 $-j3.2430$	±0.0529	±0.0659
Figure 7, $d_1/d_2 = 0.846$	-0.4077 $-j0.1252$	-0.0134 $-j58.5225$	±0.0507	±0.0687
Figure 8	$-j0.0575$	1.3486 $-j0.0142$	±0.1452	±0.1468
Figure 9	$-j0.1154$	19.7055 $-j56.7393$	±0.0073	±0.0432
Figure 12, QD	0.3346 $-j0.0008$	-40.6961 $-j20.8402$	±0.0831	±0.0202
Figure 12, CsBr	-0.0082 $-j0.1154$	22.0048 $-j54.7638$	±0.0099	±0.0431
Figure 14	0	-10.0904 $-j1.1979$	±0	±0.012
Figure 15	$-j0.0428$	-26.8103 $-j10.6391$	±0.0216	±0.0319

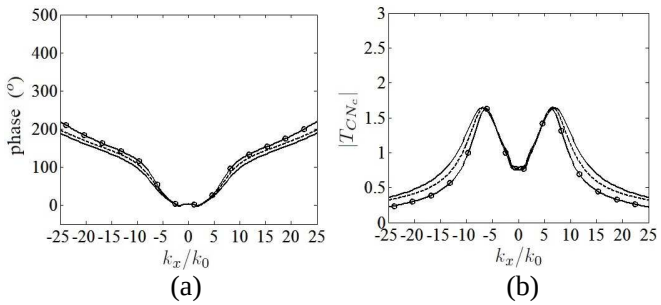

Figure 6. Effect of cell number on the transfer function: (a) phase and (b) amplitude. —: $C = 32$ (EA), $d_1/d_2 = 1$, with $\epsilon_1 = (2.3013 - j0.0014)\epsilon_0$, $\epsilon_2 = (-2.7 - j0.23)\epsilon_0$, —○—: $C = 32$ (EA), $d_1/d_2 = 1$, with $\epsilon_1 = (-2.7 - j0.23)\epsilon_0$, $\epsilon_2 = (2.3013 - j0.0014)\epsilon_0$, ---: (AA), $d_1/d_2 = 1$, $N_c = 2$, $d = 80\,\text{nm}$, $a = 20\,\text{nm}$, $w = 80\,\text{nm}$.

zero. Figure 7(a) shows the characteristics of the periodic multilayered superlenses at $d_1/d_2 = 0.846$ ($\text{Re}\{1/\epsilon_{rz}\} = 0$) and $d_1/d_2 = 1.173$ ($\epsilon'_{rx} = 0$), respectively. At either ratio, the slope of the k'_z-k_x contour becomes smaller than that in Figure 4 (curve —○—). However, the slope of the k''_z-k_x contour, as shown in Figure 7(b), is larger than that in Figure 4 (curve —○—), which constrains the k_x-bandwidth of the transfer function. The relevant parameters associated with Figure 7 are listed in Table 1.

At $d_1/d_2 = 1.173$, $|\epsilon_{rx}|$ reaches the smallest number, but $|1/\epsilon_{rz}|$ is not small enough. Similarly, at $d_1/d_2 = 0.846$, $|1/\epsilon_{rz}|$ reaches the smallest number, but $|\epsilon_{rx}|$ is not small enough. In addition, ϵ''_{rx} and $\text{Im}\{1/\epsilon_{rz}\}$ can not be reduced to zero along with their real parts. As a result, the asymptote to the k''_z-k_x contour can not have a zero slope, which in turn restricts the k_x-bandwidth of the transfer function. In comparison, when $|\epsilon_{rx}|$ is tuned to the smallest number at $d_1/d_2 = 1.173$, the corresponding transfer function renders a better image than that in Figure 4 and that at $d_1/d_2 = 0.846$.

At small k_x, (20) shows that the transfer function becomes less independent of k_x if $|\epsilon_{rx}| \to 0$, and the transfer function is not a constant if ϵ''_{rx} is not zero. Figure 7(e) (curve —) shows that a better

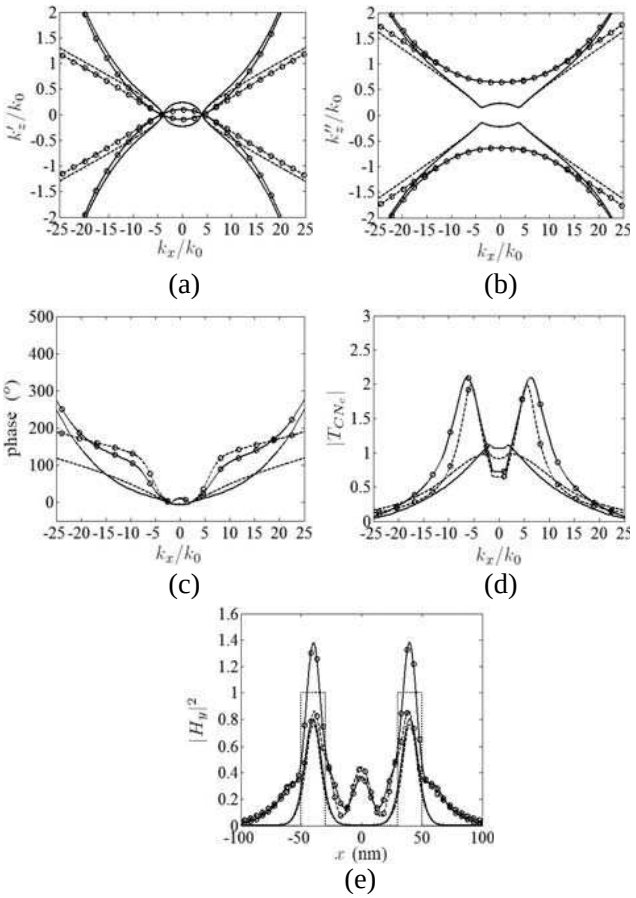

Figure 7. Effect of d_1/d_2 ratio on the characteristics of the periodic multilayered superlens, (a) k_z'-k_x contour, (b) k_z''-k_x contour, (c) phase of transfer function, (d) amplitude of transfer function, (e) recovered image. —: $C = 8$ (EA), $d_1/d_2 = 1.173$; ---: $C \to \infty$ (AA), $d_1/d_2 = 1.173$; —○—: $C = 8$ (EA), $d_1/d_2 = 0.846$; —○—: (AA), $d_1/d_2 = 0.846$; $N_c = 2$, $\epsilon_1 = (2.3013 - j0.0014)\epsilon_0$, $\epsilon_2 = (-2.7 - j0.23)\epsilon_0$, $d = 80\,\text{nm}$, $a = 20\,\text{nm}$, $w = 80\,\text{nm}$.

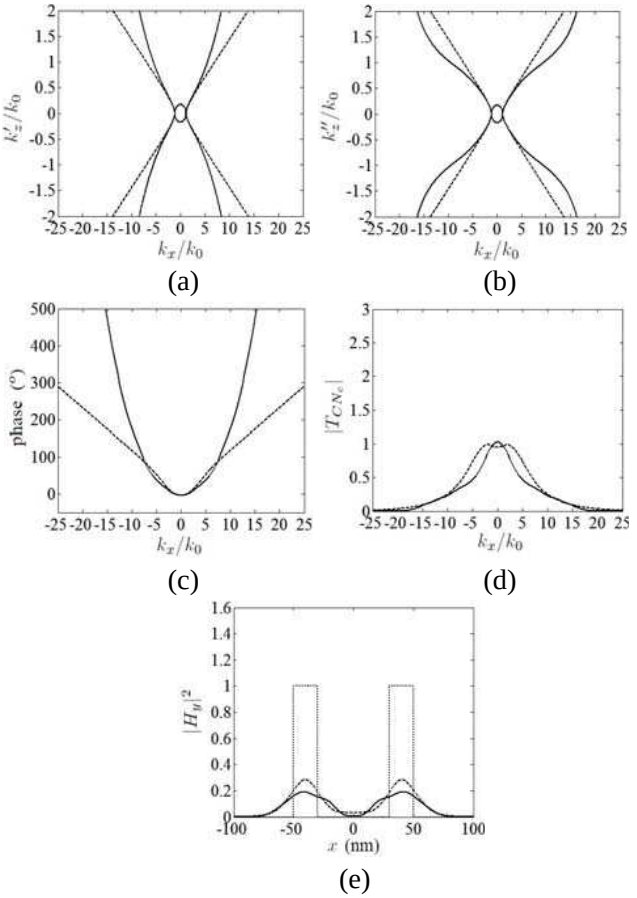

Figure 8. Effect of using a low-permittivity layer on the characteristics of the periodic multilayered superlens, (a) k_z'-k_x contour, (b) k_z''-k_x contour, (c) phase of transfer function, (d) amplitude of transfer function, (e) recovered image. —: $C = 8$ (EA), $d_1/d_2 = 3$, ---: (AA), $d_1/d_2 = 3$, $N_c = 2$, $\epsilon_1 = 0.9\epsilon_0$, $\epsilon_2 = (-2.7 - j0.23)\epsilon_0$, $d = 80\,\text{nm}$, $a = 20\,\text{nm}$, $w = 80\,\text{nm}$.

resolution is achieved when $\epsilon_{rx}' = 0$.

If a material with very small positive ϵ_r' is used to replace PMMA, d_1/d_2 has to be very large to make ϵ_{rx}' zero and ϵ_{rx}'' very small. However, large d_1/d_2 also renders a small $|\epsilon_{rz}|$, which tends to increase the slope of the asymptote to the k_z''-k_x contour, based on (16).

Figure 8 shows that, by choosing $\epsilon_1 = 0.9\epsilon_0$, a large slope of the asymptote to the k_z''-k_x contour causes the transfer function to have a narrow k_x-bandwidth. Thus, the recovered image is expected to be poor, as shown in Figure 8(e). The relevant parameters associated with Figure 8 are listed in Table 1.

5. SUPERLENSES CONTAINING CsBr LAYERS

Consider a four-layer cell, PMMA/Ag/X/Ag, where X is a DPS material with $\epsilon_3 = 3.0987\epsilon_0$, Materials X and PMMA are used to make ϵ_{rx}' close to zero. Figure 9 shows that the slope of k_z'-k_x contour decreases with the decreasing of ϵ_{rx}'. Since $|\epsilon_3| > |\epsilon_1|$, $|\epsilon_3|$ has a smaller contribution to $1/\epsilon_{rz}$, leading to

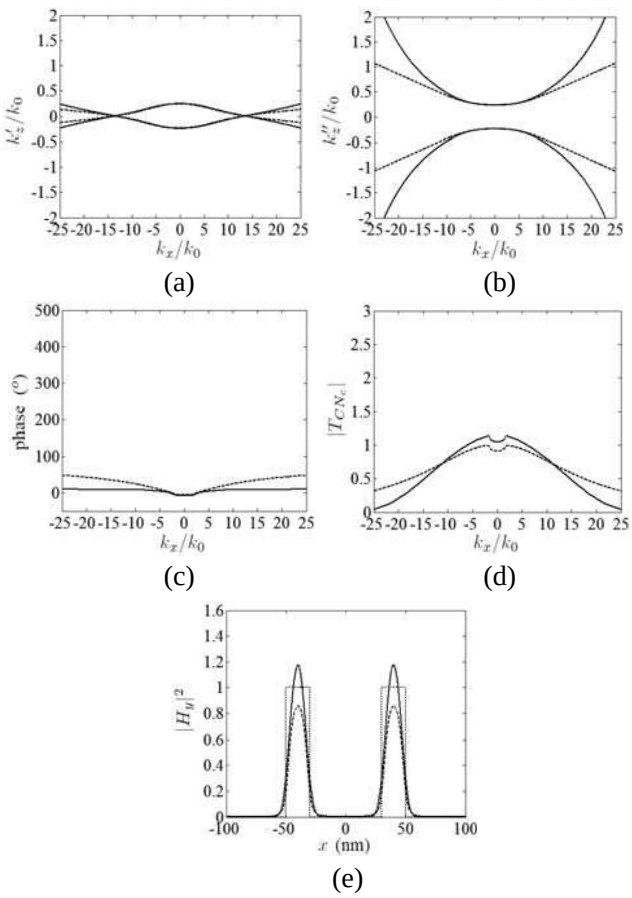

Figure 9. Effect of four-layer cell, PMMA/Ag/X/Ag, on the characteristics of the periodic multilayered superlens, (a) k_z'-k_x contour, (b) k_z''-k_x contour, (c) phase of transfer function, (d) amplitude of transfer function, (e) recovered image. —: $C = 4$ (EA), ---: (AA), $N_c = 4$, $\epsilon_1 = (2.3013 - j0.0014)\epsilon_0$, $\epsilon_2 = (-2.7 - j0.23)\epsilon_0$, $\epsilon_3 = 3.0987\epsilon_0$, $\epsilon_4 = (-2.7 - j0.23)\epsilon_0$, $d = 80\,\text{nm}$, $a = 20\,\text{nm}$, $w = 80\,\text{nm}$.

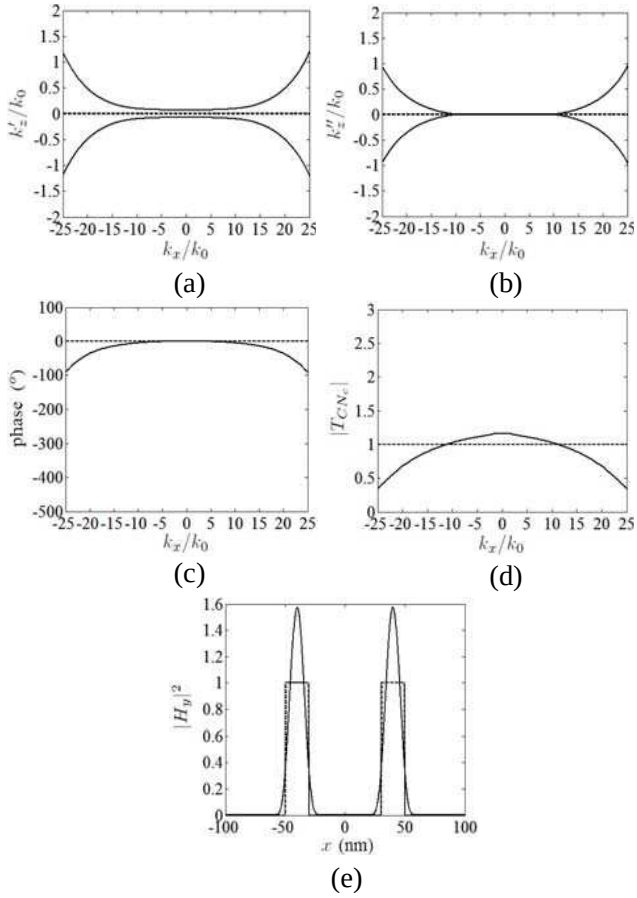

Figure 10. Effect of four-layer cell, PMMA/Ag/X/Ag, with X an active material, on the characteristics of the periodic multilayered superlens, (a) k_z'-k_x contour, (b) k_z''-k_x contour, (c) phase of transfer function, (d) amplitude of transfer function, (e) recovered image. —: $C = 4$ (EA), ---: (AA), $N_c = 4$, $\epsilon_1 = (2.3013 - j0.0014)\epsilon_0$, $\epsilon_2 = (-2.7 - j0.23)\epsilon_0$, $\epsilon_3 = (3.0987 + j0.4614)\epsilon_0$, $\epsilon_4 = (-2.7 - j0.23)\epsilon_0$, $d = 80\,\text{nm}$, $a = 20\,\text{nm}$, $w = 80\,\text{nm}$.

a larger $|\epsilon_{rz}|$. A larger $|\epsilon_{rz}|$ reduces the slope of the asymptotes to the k_z-k_x contours, based on (16). A smaller slope of the asymptote to the k_z''-k_x contour renders a wider transfer function, based on (19). In addition, small ϵ_{rx}' implies that the amplitude of the transfer function is nearly a constant at small k_x, which renders less distortion. The relevant parameters associated with Figure 9 are listed in Table 1.

Note that CsBr has a refractive index of 1.75118 at $\lambda = 365\,\text{nm}$, or $\epsilon_{\text{CsBr}} = 3.067\epsilon_0$ [23]. CsBr has a simple cubic crystal structure with lattice constant around 0.429 nm [24], which matches well with the lattice constant of Ag, 0.409 nm [25]. A 5 nm-thick CsBr layer has been fabricated before for other uses [26]. So it is feasible to use CsBr layer as the material X discussed above.

6. SUPERLENSES CONTAINING ACTIVE LAYERS

The imaginary part of ϵ_{rx} makes the transfer function less flat at small k_x, and prevents the slope of the asymptote to the k_z''-k_x contour from getting smaller. We may consider an active material for X, with $\epsilon_{rx} = 3.0978 + j0.4614$, to make ϵ_{rx} close to zero. If $\epsilon_{rx} = 0$ can be achieved, the slope of the

asymptote to the k_z''-k_x contour becomes zero, the transfer function has a wider k_x-bandwidth and a flatter amplitude at small k_x.

As shown in Figure 10, the transfer function improves as expected. With $C = 4$, the slope of asymptote to the k_z''-k_x contour is not exactly zero, hence the transfer function has a narrower k_x-bandwidth than expected. At $C \to \infty$, an almost perfect image is obtained, as shown in Figure 10(e). Note that the permittivity is a macroscopic parameter, and is not applicable if the layers are too thin.

To implement an active layer with $\epsilon = (3.0987 + j0.4614)\epsilon_0$ at $\lambda = 365\,\text{nm}$, ZnO quantum dots [27] immersed in an SiO_2 substrate [28] can be considered. The SiO_2 is also a common material to make superlenses.

The dielectric constant of a spherical quantum dot can be expressed as [29]

$$\epsilon_{r\text{QD}}(\omega) = \epsilon_{r\infty}^{i} + \frac{2f_{\text{QD}}}{V_{\text{QD}}} \frac{[f_c - f_v]e^2\xi_{\text{osc}}/m_0\epsilon_0}{\omega^2 - \omega_0^2 - j(2\omega\gamma)} \tag{21}$$

where $\epsilon_{r\infty}^{i}$ is the relative dielectric constant of the bulk ZnO material, at $\omega \to \infty$; $V_{\text{QD}} = 4\pi R_{\text{QD}}^3/3$ is the volume of one quantum dot; f_c and f_v are the electron distributions in the conduction band and the valence band, respectively; ξ_{osc} is the oscillation strength of each quantum dot; m_0 is the mass of an electron; γ is the broadening constant of a quantum dot; $\hbar\omega_0 = E_g + E_e + E_h - E_b$ is the transition energy of the quantum dot, E_g is the bandgap of the bulk material, E_e and E_h are the ground-state energy levels of the electrons and the holes, respectively, and E_b is the electron-hole binding energy; $f_{\text{QD}} = N_e V_{\text{QD}}$ is the fractional volume of the quantum dots.

A mixing formula [30] can be used to predict the dielectric constant of ZnO quantum dots immersed in the SiO_2 substrate. The difference of prediction using the different mixing formulas of Maxwell-Garnett, Bruggeman, and coherent-potential models, is not obvious when the ratio, ϵ_i/ϵ_e, is below three; where ϵ_i and ϵ_e are the permittivity of the inclusion and the substrate, respectively. In this work, $\epsilon_{\text{QD}}/\epsilon_{\text{SiO}_2}$ falls between 1 and 2. Hence, the Maxwell-Garnett mixing formula is used to predict the dielectric constant of ZnO quantum dots immersed in the SiO_2 substrate as

$$\epsilon_r^{\text{mix}}(\omega) = \epsilon_{r\infty}^{b} + \frac{3f_{\text{QD}}\epsilon_{r\infty}^{b}\left(\epsilon_{r\text{QD}} - \epsilon_{r\infty}^{b}\right)}{\epsilon_{r\text{QD}} + 2\epsilon_{r\infty}^{b} - f_{\text{QD}}\left(\epsilon_{r\text{QD}} - \epsilon_{r\infty}^{b}\right)} \tag{22}$$

where $\epsilon_{r\infty}^{b}$ is the relative dielectric constant of SiO_2 at $\omega \to \infty$. The relevant parameters are listed in Table 2 [27, 28, 31–34].

Table 2. Parameters of quantum dots.

	E_g (eV)	m_e/m_0	m_h/m_0	ϵ_s	ϵ_∞	$\hbar\omega_{\text{LO}}$ (meV)	E_P (eV)	V_e (eV)	V_h (eV)	γ (meV)
ZnO	3.37 [32]	0.3 [28]	0.8 [28]	8.5 [28]	6 [28]	73.33 [34]	28.2 [27]	4.7 [32]	0.93 [32]	1.6113 [33]
SiO_2	9 [32]	0.42 [31]	0.33 [31]	-	3.9 [28]	-	-	-	-	-

In Table 2, ϵ_s and ϵ_∞ are the static and optical permittivity, respectively; and ω_{LO} is the LO phonon frequency. These three parameters are used to solve the binding energy, E_b, of a quantum dot [35]; and ϵ_∞ is used to calculate the dielectric function of a bulk material. The Kane's energy parameter, E_P, is used to calculate the oscillation strength, ξ_{osc} [29]. The potential barriers between ZnO and SiO_2, to electrons and holes, are V_e and V_h, respectively; which are used to calculate the excited state energy level of electron and hole, E_e and E_h, respectively [29].

The radius of quantum dots is chosen as $R_{\text{QD}} = 3.52\,\text{nm}$, to render an active material centered at $\lambda = 365\,\text{nm}$. The fractional volume is $f_{\text{QD}} = 0.45$, to achieve the desired imaginary part of permittivity. For simplicity, the electron is assumed to be in the conduction band, thus, $f_c = 1$ and $f_v = 0$. As shown in Figure 11, $\epsilon = (4.473 + j0.4583)\epsilon_0$ at $\lambda = 365\,\text{nm}$.

Figure 12 shows the k_z-k_x contours, transfer function, and recovered image using the superlenses containing CsBr and active layer, respectively. The slope of the k_z'-k_x contour with the active layer is larger than that of the CsBr layer, hence the slope of phase with k_x is larger in the former case. Although the active layer can reduce the imaginary part of ϵ_{rx}, the real part of ϵ_{rx} becomes larger, implying possible distortion. The relevant parameters associated with Figure 12 are listed in Table 1.

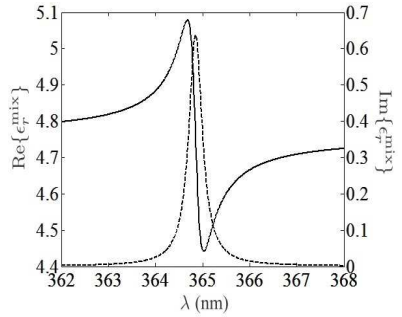

Figure 11. Effective dielectric constant of ZnO quantum dots immersed in the SiO_2 substrate with $f_c = 1$, and $f_v = 0$. —: real part, ---: imaginary part.

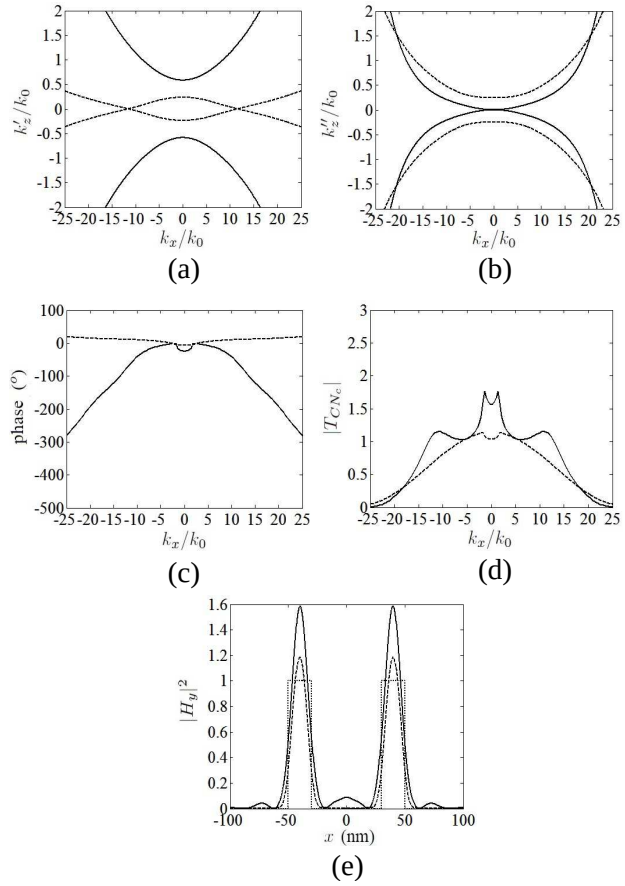

Figure 12. Characteristics of periodic multilayered superlens with four-layer cell, PMMA/Ag/X/Ag, with X = CsBr or ZnO QD's in SiO_2, (a) k_z'-k_x contour, (b) k_z''-k_x contour, (c) phase of transfer function, (d) amplitude of transfer function, (e) recovered image. $N_c = 4$, $C = 4$, $d = 80\,\text{nm}$, $a = 20\,\text{nm}$, $w = 80\,\text{nm}$, $d_1 = d_2 = d_3 = d_4$, $\epsilon_1 = (2.3013 - j0.0014)\epsilon_0$, $\epsilon_2 = \epsilon_4 = (-2.7 - j0.23)\epsilon_0$, —: $\epsilon_3 = (4.437 + j0.4583)\epsilon_0$ (ZnO quantum dots in SiO_2), ---: $\epsilon_3 = 3.067\epsilon_0$ (CsBr).

Since the radius of a QD is $R_{\text{QD}} = 3.52\,\text{nm}$, the thickness of the QD layer should be larger than $2R_{\text{QD}}$. Otherwise, the dielectric constant will deviate from its designed value. In order to stretch the tuning range of thickness of the active layer, the cell number is halved and the thickness of each layer is doubled, while maintaining the same total thickness, d. However, the transfer function of the superlens will deviate from the original design, and its k_x-bandwidth can be reduced. The transfer function and

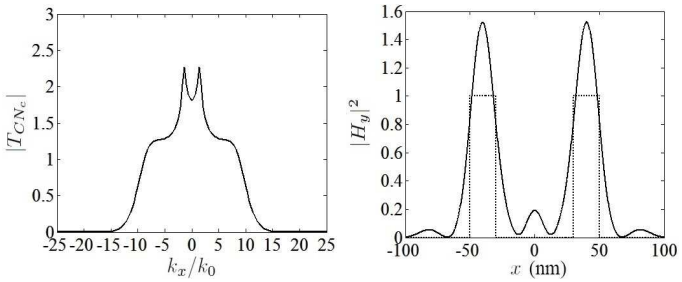

Figure 13. Characteristics of two-cell four-layer superlens containing active layers: (a) amplitude of transfer function and (b) recovered image. —: $C = 2$, $d_1 = d_2 = d_3 = d_4 = 10\,\text{nm}$, with $\epsilon_1 = (2.3013 - j0.0014)\epsilon_0$, $\epsilon_2 = \epsilon_4 = (-2.7 - j0.23)\epsilon_0$, $\epsilon_3 = (4.437 + j0.4583)\epsilon_0$, $N_c = 4$, $d = 80\,\text{nm}$, $a = 20\,\text{nm}$, $w = 80\,\text{nm}$.

the recovered image are shown in Figure 13.

Next, by adjusting the thickness of each layer in a cell, with $C = 2$, a smallest possible ϵ_{rx} is achieved at $d_1 = 4.791\,\text{nm}$, $d_2 = d_4 = 11.717\,\text{nm}$ and $d_3 = 11.775\,\text{nm}$. The simulation results are shown in Figure 14, and the relevant parameters are listed in Table 1. It is observed that the AA predicts a perfect resolution, but the EA predicts quite differently, in the k_z-k_x contours, the transfer function and the recovered image. The recovered image displays an obvious distortion, which is related to the wild variation of the transfer function.

The peaks in the transfer function indicate the existence of resonant modes in the superlens. These resonant modes are suppressed in the original superlens design with an effective lossy medium. When the loss in silver and PMMA layers is compensated by the active layers, these resonant modes emerge under proper conditions. The effect of resonant modes can not be modeled with AA, based on the effective medium theory.

In order to suppress the the resonant modes, we need to introduce a small loss to ϵ_{rx}, while the thickness of the active layer is set to a threshold value of 7.04 nm. By solving (13), with the goal to reach $\epsilon'_{rx} = 0$, we obtain $\epsilon''_{rx} = -0.0428$, $d_1 = 11.5384\,\text{nm}$, $d_2 = d_4 = 10.7074\,\text{nm}$ and $d_3 = 7.0468\,\text{nm}$. Figure 15 shows the simulation results with these parameters, and the relevant parameters are listed in Table 1.

The recovered image and the transfer function are improved over those in Figure 14, with $\epsilon_{rx} = 0$. The peaks of the transfer function in Figure 14, caused by the resonant modes, are suppressed by the loss medium. The k_z-k_x contours predicted with the EA look closer to those with the AA, as compared to those shown in Figure 14. However, since only two cells are used, the k''_z-k_x contour with the EA is still different from that with the AA. The k''_z-k_x contour rises quickly with k_x, hence the k_x-bandwidth of the transfer function is reduced.

Figure 16 shows the recovered image with half-pitch of $\lambda/20$, using the three superlenses simulated in Sections 4, 5 and 6, respectively. The superlens of two-layer cells simulated in Section 4 renders the worst quality, while that with CsBr-layer renders the best quality. The superlenses with four-layer cells, simulated in Sections 5 and 6, can resolve an image with $\lambda/20$ half-pitches, finer than those in the literatures [2–13].

Finally, the superlens containing CsBr layers is applied to resolve an even finer image, with half-pitch of $\lambda/36$, and the result is shown in Figure 17.

7. TOLERANCE ANALYSIS

The optimal designs may be affected by two possible errors, the wavelength deviation of the laser and the thickness deviation in the fabrication process. The permittivity of materials is a function of wavelength, and a practical laser source has a finite linewidth. The linewidth of a tunable laser with the wavelength range of 350–370 nm has been reduced to the order of 0.01 nm [36]. Many laser sources

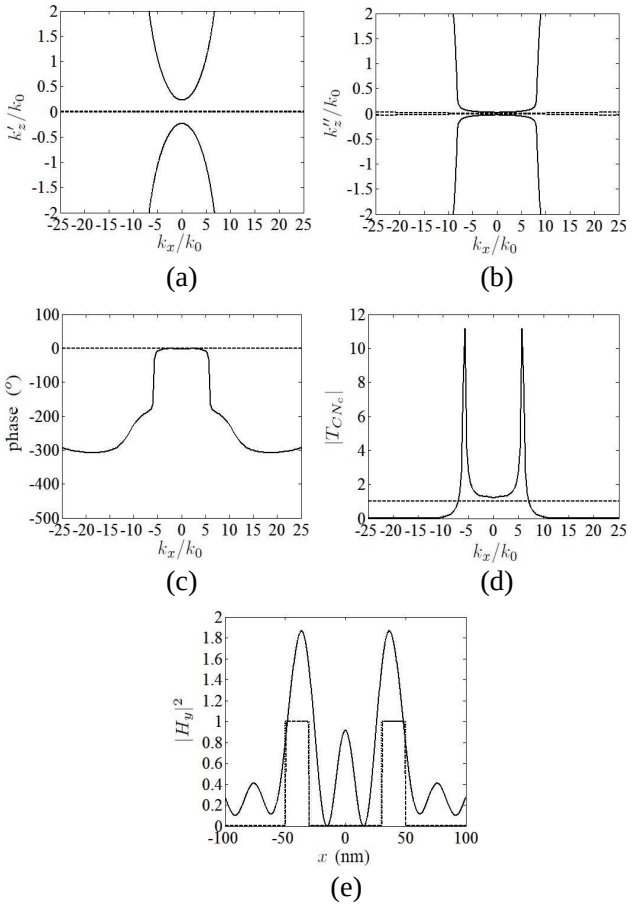

Figure 14. Characteristics of PMMA/Ag/QD/Ag periodic multilayered superlens with $\epsilon_{rx} = 0$, (a) k_z'-k_x contour, (b) k_z''-k_x contour, (c) phase of transfer function, (d) amplitude of transfer function, (e) recovered image. $N_c = 4$, $C = 2$, $d = 80\,\text{nm}$, $a = 20\,\text{nm}$, $w = 80\,\text{nm}$, $d_1 = 4.791\,\text{nm}$, $d_2 = d_4 = 11.717\,\text{nm}$, $d_3 = 11.775\,\text{nm}$, $\epsilon_1 = (2.3013 - j0.0014)\epsilon_0$, $\epsilon_2 = \epsilon_4 = (-2.7 - j0.23)\epsilon_0$, $\epsilon_3 = (4.437 + j0.4583)\epsilon_0$ (ZnO quantum dots in SiO_2), —: EA, ---: AA.

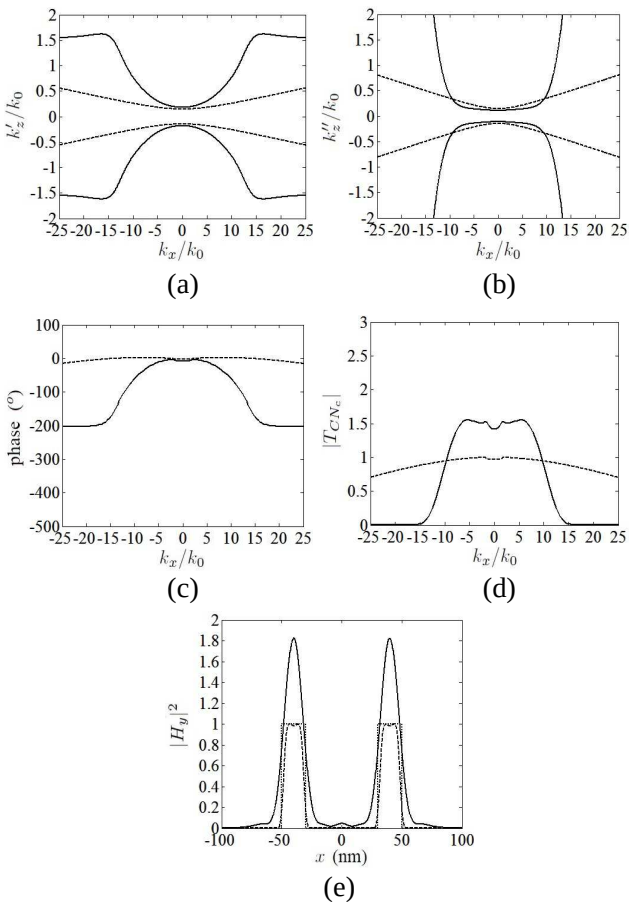

Figure 15. Characteristics of PMMA/Ag/QD/Ag periodic multilayered superlens with $\epsilon_{rx} = -j0.0428\epsilon_0$, (a) k_z'-k_x contour, (b) k_z''-k_x contour, (c) phase of transfer function, (d) amplitude of transfer function, (e) recovered image. $N_c = 4$, $C = 2$, $d = 80\,\text{nm}$, $a = 20\,\text{nm}$, $w = 80\,\text{nm}$, $d_1 = 11.5384\,\text{nm}$, $d_2 = d_4 = 10.7074\,\text{nm}$, $d_3 = 7.0468\,\text{nm}$, $\epsilon_1 = (2.3013 - j0.0014)\epsilon_0$, $\epsilon_2 = \epsilon_4 = (-2.7 - j0.23)\epsilon_0$, $\epsilon_3 = (4.437 + j0.4583)\epsilon_0$ (ZnO quantum dots in SiO_2), —: EA, ---: AA.

have been designed to have a linewidth of 0.0005 nm around the wavelength of 600 nm [37]. We will choose a linewidth deviation of 0.001 nm to study its effect on the optimal design.

Figure 18 shows the wavelength dependence of permittivity of Ag, PMMA, CsBr and QD layer, respectively. For Ag, PMMA and CsBr, if the wavelength is shifted by 0.001 nm from 365 nm, the permittivity deviation is on the order of 10^{-5} or smaller, which can be ignored. For QD layer, the real part of permittivity varies on the order of 0.001, and the imaginary part varies in the range of 0.4559–0.4607; which can also be ignored. In summary, the performance of our superlenses is barely affected if the wavelength shift of the laser sources is limited to 0.001 nm.

Next, we consider the effects of thickness deviation due to fabrication. Thin-film Ag and PMMA can be deposited using different methods, with the deposition rate of one nanometer per second [39, 40]. It is reasonable to assume that the thickness deviation of each layer is either 1 nm thicker or 1 nm thinner than the original design.

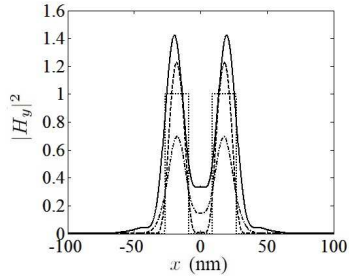

Figure 16. Comparison of recovered images ($a = 18\,\text{nm}$, $w = 36\,\text{nm}$) with three superlenses: —: $N_c = 4$, $C = 2$, $d_1 = 11.5384\,\text{nm}$, $d_2 = d_4 = 10.7074\,\text{nm}$, $d_3 = 7.0468\,\text{nm}$, $\epsilon_1 = (2.3013 - 0.0014j)\epsilon_0$, $\epsilon_3 = (4.437 + j0.4583)\epsilon_0$ (QD), $\epsilon_2 = \epsilon_4 = (-2.7 - j0.23)\epsilon_0$. ---: $N_c = 4$, $C = 4$, $d_1 = d_2 = d_3 = d_4 = 5\,\text{nm}$, $\epsilon_1 = (2.3013 - 0.0014j)\epsilon_0$, $\epsilon_3 = 3.067\epsilon_0$ (CsBr), $\epsilon_2 = \epsilon_4 = (-2.7 - j0.23)\epsilon_0$. —·—: $N_c = 2$, $C = 8$, $d_1/d_2 = 1.173$, $\epsilon_1 = (2.3013 - j0.0014)\epsilon_0$, $\epsilon_2 = (-2.7 - j0.23)\epsilon_0$.

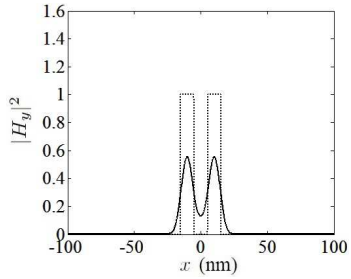

Figure 17. Recovered image ($a = 10\,\text{nm}$, $w = 20\,\text{nm}$) with superlenses: $N_c = 4$, $C = 4$, $\epsilon_1 = (2.3013 - j0.0014)\epsilon_0$, $\epsilon_3 = 3.067\epsilon_0$ (CsBr), $\epsilon_2 = \epsilon_4 = (-2.7 - j0.23)\epsilon_0$.

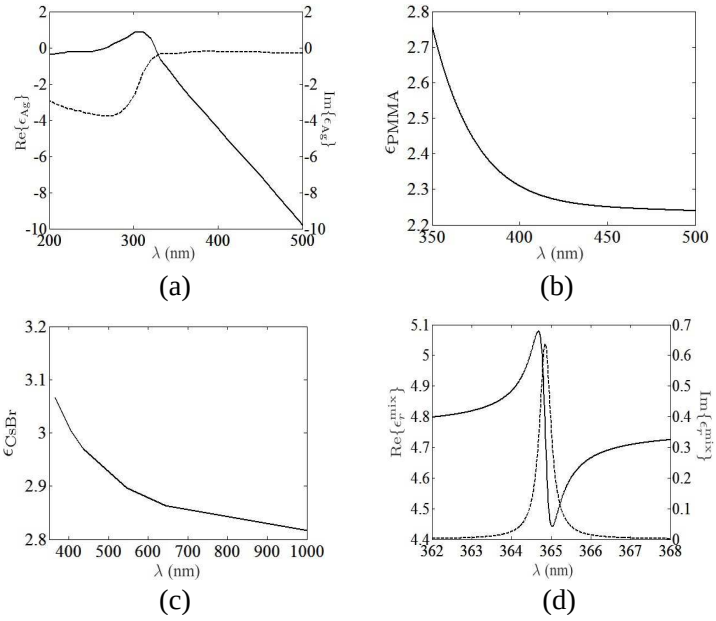

Figure 18. Wavelength dependence of permittivity: (a) Ag [21], (b) PMMA [38], (c) CsBr [23], (d) QD layer (also shown in Figure 11).

Figure 19 shows the recovered images using the superlens made of two-layered (PMMA/Ag) cells, with the same parameters as in Figure 7. With the thickness variation of $\pm 1\,\text{nm}$ in each layer, only a very small variation is observed.

Figure 20 shows the recovered image using the superlens made of four-layered (PMMA/Ag/CsBr/Ag) cells, with the same parameters as in Figure 12. With the thickness variation of $\pm 1\,\text{nm}$ in each layer, only a very small variation is observed.

Figure 21 shows the recovered image using the superlens made of four-layered (PMMA/Ag/QD/Ag) cells, with the same parameters as in Figure 15. Since the QD layer can not be thinner than the QD's diameter, only the thickness variation of 1 nm in each layer is considered. The variation is larger than those in Figures 19 and 20.

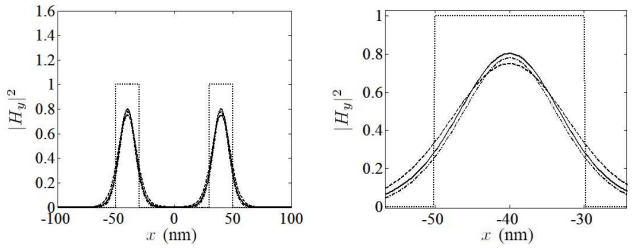

Figure 19. Variation of recovered image using the superlens made of two-layered (PMMA/Ag) cells: (a) full-scale image, (b) enlarged portion around one window; —: with the parameters of — curve in Figure 7; ---: with the same parameters except each layer is 1 nm thicker; —·—: with the same parameters except each layer is 1 nm thinner.

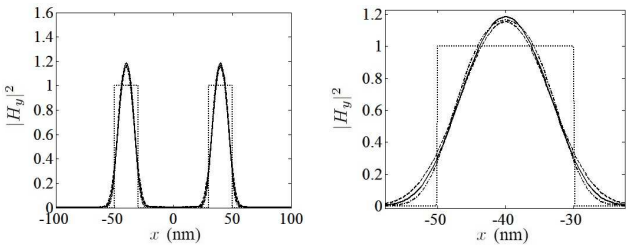

Figure 20. Variation of recovered image using the superlens made of four-layered (PMMA/Ag/CsBr/Ag) cells: (a) full-scale image, (b) enlarged portion around one window; —: with the parameters of --- curve in Figure 12; ---: with the same parameters except each layer is 1 nm thicker; —·—: with the same parameters except each layer is 1 nm thinner.

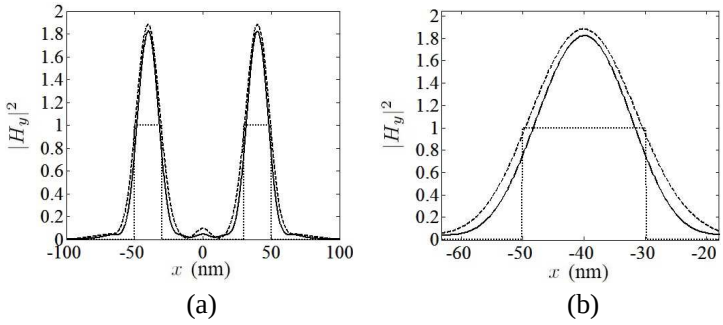

Figure 21. Variation of recovered image using the superlens made of four-layered (PMMA/Ag/QD/Ag) cells: (a) full-scale image, (b) enlarged portion around one window; —: with the parameters of — curve in Figure 15; ---: with the same parameters except each layer is 1 nm thicker.

In summary, under reasonable thickness tolerance of the fabrication process and reasonable wavelength tolerance of the laser source, the optimal designs of superlens are only slightly affected.

8. CONCLUSION

A transfer-matrix approach is proposed to derive the transfer function of periodic multilayered superlenses, composed of passive or active layers. The effective medium theory is applied to derive the dispersion relation, to explore possible resolution improvement. Both the real and the imaginary parts of the k_z-k_x contours are used to analyze the phase variation and the k_x-bandwidth of the transfer function. CsBr layers are proposed to equalize the transfer function at small k_x's to effectively reduce the image distortion. To compensate for the material loss, active layers are proposed, which are SiO_2 substrate embedded with ZnO quantum dots. The proposed superlenses can resolve half-pitch features of $\lambda/36$ using the CsBr layers, or $\lambda/20$ using the active layers. A tolerance analysis indicates that the performance of the proposed superlenses is only slightly affected by reasonable deviations of layer thickness and wavelength.

ACKNOWLEDGMENT

This work was sponsored by the National Science Council, Taiwan, R.O.C., under contract NSC 100-2221-E-002-232.

REFERENCES

1. Engheta, N. and R. W. Ziolkowski, *Electromagnetic Metamaterials: Physics and Engineering Explorations*, IEEE Press, 2006.
2. Pendry, J. B., "Negative refraction makes perfect lens," *Phys. Rev. Lett.*, Vol. 85, No. 18, 3966–3969, 2000.
3. Shi, Z., V. Kochergin, and F. Wang, "193 nm superlens imaging structure for 20 nm lithography node," *Opt. Exp.*, Vol. 17, No. 14, 11309–11314, 2009.
4. Fang, N., H. Lee, C. Sun, and X. Zhang, "Sub-diffraction-limited optical imaging with a silver superlens," *Science*, Vol. 308, No. 5721, 534–537, 2005.
5. Ramakrishna, S. A. and J. B. Pendry, "Imaging the near field," *J. Mod. Opt.*, Vol. 50, No. 9, 1419–1430, 2003.
6. Li, G., J. Li, H. L. Tam, C. T. Chan, and K. W. Cheah, "Sub-wavelength imaging from multilayer superlens," *Int. Nanoelectron. Conf.*, 1309–1310, 2010.
7. Melville, D. O. S. and R. J. Blaikie, "Analysis and optimization of multilayer silver superlenses for near-field optical lithography," *Physica B*, Vol. 394, No. 2, 197–202, 2007.
8. Wood, B. and J. B. Pendry, "Directed subwavelength imaging using a layered metal-dielectric system," *Phys. Rev. B*, Vol. 74, No. 11, 115116, 2006.
9. Xu, T., Y. Zhao, J. Ma, C. Wang, J. Cui, C. Du, and X. Luo, "Sub-diffraction-limited interference photolithography with metamaterials," *Opt. Exp.*, Vol. 16, No. 18, 13579–13584, 2008.
10. Wang, C., Y. Zhao, D. Gan, C. Du, and X. Luo, "Subwavelength imaging with anisotropic structure comprising alternately layered metal and dielectric films," *Opt. Exp.*, Vol. 16, No. 6, 4217–4227, 2008.
11. Scalora, M., G. D'Aguanno, N. Mattiucci, and M. J. Bloemer, "Negative refraction and sub-wavelength focusing in the visible range using transparent metallodielectric stacks," *Opt. Exp.*, Vol. 15, No. 2, 508–523, 2007.
12. Moore, C. P., "Optical superlenses: Quality and fidelity in silver-dielectric near-field imaging systems," University of Canterbury, May 24, 2011.
13. Xie, Z., W. Yu, T. Wang, H. Zhang, Y. Fu, H. Liu, F. Li, Z. Lu, and Q. Sun, "Plasmonic nanolithography: A review," *Plasmonics*, Vol. 6, 565–580, 2011.
14. Liu, Z., S. Durant, H. Lee, Y. Pikus, N. Fang, Y. Xiong, C. Sun, and X. Zhang, "Far-field optical superlens," *Nano Lett.*, Vol. 7, No. 2, 403–408, 2006.
15. Lee, H., Z. Liu, Y. Xiong, C. Sun, and X. Zhang, "Design, fabrication and characterization of a far-field superlens," *Solid State Commun.*, Vol. 146, 202–207, 2008.
16. Cao, P. F., X. P. Zhang, L. Cheng, and Q. Q. Meng, "Far field imaging research based on multilayer positive- and negative-refractive-index media under off-axis illumination," *Progress In Electromagnetics Research*, Vol. 98, 283–298, 2009.
17. Smolyaninov, I. I., Y.-J. Hung, and C. C. Davis, "Magnifying superlens in the visible frequency range," *Science*, Vol. 315, No. 5819, 1699–1701, 2007.
18. Cheng, B. H., Y. Z. Ho, Y.-C. Lan, and D. P. Tsai, "Optical hybrid-superlens hyperlens for superresolution imaging," *IEEE J. Sel. Top. Quantum Electron.*, Vol. 19, No. 3, 2013.
19. Kiang, J.-F., S. M. Ali, and J. A. Kong, "Integral equation solution to the guidance and leakage properties of coupled dielectric strip waveguides," *IEEE Trans. Microwave Theory Tech.*, Vol. 38, No. 2, 193–203, Feb. 1990.
20. Born, M. and E. Wolf, *Principles of Optics*, Pergamon Press, Oxford, 1980.
21. Johnson, P. B. and R. W. Christy, "Optical constants of the noble metals," *Phys. Rev. B*, Vol. 6, No. 12, 4370–4379, 1972.
22. Mitra, S. K. and S. Chakraborty, *Microfluidics and Nanofluidics Handbook: Fabrication, Implementation, and Applications*, CRC Press, 2012.
23. Rodney, W. S. and R. J. Spindler, "Refractive index of cesium bromide for ultraviolet, visible, and infrared wavelengths," *J. Res. Bur. Stand.*, Vol. 51, No. 3, 123–126, 1953.

24. Buzulutskovl, A., E. Shefer, A. Breskin, R. Chechik, and M. Prager, "The protection of K-Cs-Sb photocathodes with CsBr films," *Nuclear Instru. Methods Phys. Res. A*, Vol. 400, 173–176, 1997.
25. Wasserman, H. J. and J. S. Vermaak, "On the determination of a lattice contraction in very small silver particles," *Surface Science*, Vol. 22, 164–172, 1970.
26. Maldonado, J. R., P. Pianetta, D. H. Dowell, J. Smedley, and P. Kneisel, "Performance of a CsBr coated Nb photocathode at room temperature," *J. Appl. Phys.*, Vol. 107, 013106, 2010.
27. Fonoberov, V. A. and A. A. Balandin, "ZnO quantum dots: Physical properties and optoelectronic applications," *J. Nanoelectron. Optoelectron.*, Vol. 1, 19–38, 2006.
28. Peng, Y.-Y., T.-E. Hsieh, and C.-H. Hsu, "Dielectric confinement effect in ZnO quantum dots embedded in amorphous SiO_2 matrix," *J. Phys. D: Appl. Phys.*, Vol. 40, 6071–6075, 2007.
29. Holmstrom, P., L. Thylen, and A. Bratkovsky, "Dielectric function of quantum dots in the strong confinement regime," *J. Appl. Phys.*, Vol. 107, No. 6, 064307, 2010.
30. Sihvola, A. *Electromagnetic Mixing Formulas and Applications*, IEE, London, 1999.
31. Vexler, M. I., S. E. Tyaginov, and A. F. Shulekin, "Determination of the hole effective mass in thin silicon dioxide film by means of an analysis of characteristics of a MOS tunnel emitter transistor," *J. Phys.: Condens. Matter*, Vol. 17, 8057–8068, 2005.
32. You, J. B., X. W. Zhang, H. P. Song, J. Ying, Y. Guo, A. L. Yang, Z. G. Yin, N. F. Chen, and Q. S. Zhu, "Energy band alignment of SiO_2/ZnO interface determined by X-ray photoelectron spectroscopy," *J. Appl. Phys.*, Vol. 106, 043709, 2009.
33. Ellmer, K., A. Klein, and B. Rech, *Transparent Conductive Zinc Oxide: Basics and Applications in Thin Film Solar Cells*, Springer, 2008.
34. Alim, K. A., V. A. Fonoberov, and A. A. Balandin, "Interpretation of the phonon frequency shifts in ZnO quantum dots," *Matter. Res. Soc. Symp.*, Vol. 872, J13.21, 2005.
35. Pellegrini, G., G. Mattei, and P. Mazzoldi, "Finite depth square well model: Applicability and limitations," *J. Appl. Phys.*, Vol. 97, 073706, 2005.
36. Stokes, E. D., F. B. Dunning, R. F. Stebbings, G. K. Walters, and R. D. Rundel, "A high efficiency dye laser tunable from UV to the IR," *Opt. Commun.*, Vol. 5, No. 4, 267–270, 1972.
37. Duarte, F. J., "Tunable organic dye lasers: Physics and technology of high-performance liquid and solid-state narrow-linewidth oscillators," *Prog. Quantum Electron.*, Vol. 36, 29–50, 2012.
38. Kasarova, S. N., N. G. Sultanova, C. D. Ivanov, and I. D. Nikolov, "Analysis of the dispersion of optical plastic materials," *Opt. Mater.*, Vol. 29, 1481–1490, 2007.
39. Melpignano, P., C. Cioarec, R. Clergereaux, N. Gherardi, C. Villeneuve, and L. Datas, "E-beam deposited ultra-smooth silver thin film on glass with different nucleation layers: An optimization study for OLED micro-cavity application," *Organic Electron.*, Vol. 11, 1111–1119, 2010.
40. Tsai, T.-C. and D. Staack, "Low-temperature polymer deposition in ambient air using a floating-electrode dielectric barrier discharge jet," *Plasma Process. Polym.*, Vol. 8, 523–534, 2011.